Biomaterials 331 (2026) 124101

Contents lists available at ScienceDirect

Biomaterials

journal homepage: www.elsevier.com/locate/biomaterials

A VITA Index for predicting cytocompatibility of metallic biomaterials based on ion release and toxicity

Tadaaki Matsuzaka, Aira Matsugaki, Takayoshi Nakano *

Division of Materials and Manufacturing Science, Graduate School of Engineering, The University of Osaka, 2-1 Yamadaoka, Suita, Osaka, 565-0871, Japan

ARTICLE INFO

Keywords:
In vitro cytocompatibility
VITA Index (Velocity–Ion Toxicity–Affinity)
Metal ion toxicity
Biomedical alloys design
Osteoblast response
Corrosion behavior

ABSTRACT

Biocompatibility and cytocompatibility are critical early considerations in the development of metallic biomaterials for implantable devices; however, conventional *in vitro* cytotoxicity evaluations typically assess corrosion behavior or cytotoxicity independently and fail to account for their coupled effects on metal-ion release–driven cytocompatibility. Here, we present a novel Velocity–Ion Toxicity–Affinity (VITA) Index—a quantitative and mechanistically informed framework that integrates electrochemical dissolution (corrosion) behavior with ion-specific cytotoxicity to evaluate *in vitro* biocompatibility governed by metal-ion release. By combining corrosion profiling with cell-based cytocompatibility assays (using osteoblasts and fibroblasts as a representative model), the VITA Index demonstrates first-order accuracy, capturing robust correlations between ion-release kinetics and cell viability across both established biomedical alloys and emerging materials, including high-entropy alloys. The VITA Index enables rapid and mechanistically informed screening of candidate metallic biomaterials and provides a practical framework for *in vitro* biocompatibility assessment, cytotoxicity prediction, and data-driven alloy design for future implant applications.

1. Introduction

The long-term success of biomedical implants depends critically on the cytocompatibility of their constituent metallic materials. Owing to their direct interface with living tissues, even minor deviations in cellular responses may contribute to chronic inflammation and impaired device function. Titanium (Ti) and stainless steel remain widely used owing to their favorable mechanical properties and corrosion resistance [1,2]. However, newly developed multi-element biomedical alloys have been developed to enable precise tuning of properties and the introduction of new functionalities [3–6]. The rational and strategic advancement of such materials is fundamentally impeded by the lack of a unified, mechanistically grounded framework for evaluating *in vitro* cytocompatibility based on ion release.

In biological environments, metals do not remain inert solids but undergo electrochemical corrosion, releasing ions, forming oxide films, and engaging in complex interactions with proteins, cells, and tissues [7–9]. These processes are acutely sensitive to local microenvironmental parameters, such as pH, chloride ion concentration, and protein adsorption, and exhibit substantial variation across different elements [10–12]. While decades of foundational studies have established robust frameworks for evaluating the biocompatibility of metallic biomaterials, these complex, time-dependent electrochemical interactions at the cell–material interface are not fully captured by conventional *in vitro* cytotoxicity assays alone [13–16].

Conventionally, assessment has relied on IC_{50} values, which quantify the concentration of metal ions that reduces cell viability by 50% [5,6,17–20]. Although IC_{50} originated as a pharmacological metric for dose-dependent inhibition of cellular functions by drugs or toxins and is useful for evaluating the cytotoxicity of dissolved ions in solution, it does not capture material-specific dynamics that govern ion release, such as corrosion rate under physiological conditions. From a materials-design standpoint, this discrepancy is substantial, as the dissolution behavior intrinsic to each metal is decoupled from the observed *in vitro* cytocompatibility.

To bridge this conceptual and methodological gap, we propose a novel Velocity–Ion Toxicity–Affinity (VITA) Index, a mechanistically informed, quantitative metric that integrates corrosion rate–driven ion release with ion-specific cytotoxicity. Beyond serving merely as an acronym, “VITA” (Latin for “life”) encapsulates the objective of guiding

* Corresponding author.
E-mail addresses: matsuzaka@mat.eng.osaka-u.ac.jp (T. Matsuzaka), matsugaki@mat.eng.osaka-u.ac.jp (A. Matsugaki), nakano@mat.eng.osaka-u.ac.jp (T. Nakano).

https://doi.org/10.1016/j.biomaterials.2026.124101
Received 31 October 2025; Received in revised form 30 January 2026; Accepted 25 February 2026
Available online 4 March 2026

the design of metallic materials that actively harmonize with biological systems; here, "Velocity" denotes the corrosion rate under physiological conditions, "Ion Toxicity" represents the cytotoxic threshold concentration, and "Affinity" indicates the predicted *in vitro* cytocompatibility. The VITA Index is defined as the ratio of the IC_{50} value to the corrosion current density (Velocity), thereby encapsulating both the corrosion-rate–dependent dissolution profile and the ion-specific toxicity profile characteristic of each element. We demonstrate that the VITA Index exhibits a strong quantitative correlation with osteoblast viability and, on the basis of this relationship, facilitates first-order prediction of metal–cell affinity. Moreover, this innovative framework complements conventional approaches, demonstrates potential applicability to established biomedical metallic alloys, and is readily applicable to multicomponent systems such as high-entropy alloys (HEAs).

The VITA Index serves as an element-level screening framework for materials design, enabling systematic evaluation of *in vitro* cytocompatibility at the elemental scale. When integrated with artificial intelligence (AI)-driven exploration, high-throughput screening, and computational materials design, this framework has the potential to facilitate more efficient and rational early-stage development of candidate biomaterials.

2. Materials and methods

2.1. Preparation of test materials

The samples used in this study were bar-shaped materials sourced from Nilaco (Tokyo, Japan); Fe, Ni, V, and Zr were 2 N, and the rest were 3 N purity. The specimens were cut to create 1 mm thick disks. The specimens for corrosion tests were mechanically polished with SiC paper 400, 800, 1200, 2000, and 4000 grades, respectively, in that order. The specimens for cell tests were further polished to a mirror finish to eliminate the influence of surface topography on cell behavior. Polished specimens were cleaned in an ultrasonic cleaner using acetone, ethanol, and distilled water and sterilized by autoclaving.

2.2. Electrochemical tests

The experimental device for carrying out electrochemical experiments was a traditional three-electrode electrochemical cell. A metallic specimen, featuring a surface area of 0.5 cm^2, was designated as the working electrode, a platinum wire served as the counter electrode, and an Ag/AgCl electrode functioned as the reference. The electrochemical cell was immersed in 50 mL of αMEM (alpha Minimum Essential Medium) and maintained at a physiological temperature of 37 °C using a thermostatic chamber. The solution underwent degassing with Ar. Electrochemical measurements were conducted using the Potentiostat HZ-Pro S4 (manufactured by MEIDEN HOKUTO CORPORATION, Tokyo, Japan) and associated software (Hoktnet Client, Hoktnet Analyzer). The specimens were allowed to stabilize at open circuit potential (OCP) for up to 60 min, until the potential variation became within ±1 mV [21,22]. Corrosion potential (E_{corr}), corrosion current (I_{corr}), and Tafel slope for anode (β_a) and cathode (β_c) were determined using Tafel's extrapolation method, ranging from −250 mV to +250 mV (vs Ag/AgCl) at a scan rate of 0.5 mV/s, with n = 5 replicates for each specimen [21–23]. This scan rate was selected to ensure stable Tafel analysis and to minimize electrode surface changes in serum-containing media.

2.3. Isolation and culture of primary osteoblasts

Primary osteoblasts were isolated through sequential enzymatic processing from calvariae of newborn C57BL/6 mice (3 days old). The surrounding fibrous tissues were meticulously removed, and the bones were finely dissected and washed in Hank's balanced salt solution (Gibco). These phases were performed in ice-cold conditions. Subsequently, the extracted calvaria were treated with collagenase/trypsin (collagenase: Wako, Osaka, Japan; trypsin: Nacalai Tesque, Kyoto, Japan) at 37 °C in 15-min intervals for five cycles. The supernatants from the first two treatments were discarded, while those from the third, fourth, and fifth treatments were collected in α-MEM (Invitrogen, Carlsbad, CA). The collected solution was passed through a 100 μm mesh strainer (BD Biosciences, San Jose, CA, USA), centrifuged to remove the supernatant, and the isolated cells were resuspended in α-MEM containing 10% fetal bovine serum (FBS; Gibco), 1% penicillin, and streptomycin (Invitrogen, Carlsbad, CA) for cell culture. All animal experiments were conducted with the approval of the University of Osaka Committee for Animal Experimentation. The isolated osteoblasts were cultured at 37 °C in 5% CO_2. L929 mouse fibroblast cells (RCB1451, RIKEN Cell Bank, Japan) were cultured according to the protocol provided by the cell bank. Cells were maintained in Minimum Essential Medium (MEM) supplemented with 5% calf serum (CS) and 1% penicillin–streptomycin, at 37 °C in a humidified atmosphere containing 5% CO_2. The culture medium was replaced every 2–3 days, and cells were subcultured using trypsin prior to reaching confluence.

2.4. Cell toxicity evaluations

Cell toxicity evaluations were calculated over time at 1, 3, and 7 days after seeding the samples on the metal substrates. Osteoblasts were seeded at 8000 cells/cm^2 on each substrate, and L929 mouse fibroblast cells were seeded at the same cell density to enable direct comparison between cell types. Nuclei and cell cytoskeletons were stained using SPY550-DNA (Cytoskeleton, Inc., Colorado, USA) and SPY650-FastAct (Cytoskeleton, Inc., Colorado, USA), respectively. The number of cells was counted, and cell viability was normalized based on the number of cells on Ti cultured for 1 day.

2.5. Immunofluorescence staining

Osteoblasts were fixed in 4% paraformaldehyde in PBS for 20 min at room temperature and permeabilized with PBST (PBS containing 0.05% Triton X-100). Non-specific binding was blocked by incubation with PBST supplemented with 1% normal goat serum (Invitrogen) for 30 min. For vinculin detection, cells were incubated overnight at 4 °C with mouse monoclonal *anti*-vinculin antibodies (Sigma-Aldrich), followed by Alexa Fluor 546-conjugated anti-mouse IgG secondary antibodies (Invitrogen) and DAPI (Invitrogen) for 2 h at room temperature. F-actin was visualized using Alexa Fluor 488-conjugated phalloidin (Invitrogen). After final washes with PBST, samples were mounted in ProLong Diamond Antifade Reagent (Invitrogen) and imaged with a fluorescence microscope (BZ-X710, Keyence, Osaka, Japan).

2.6. Analysis of elemental leachability through inductively coupled plasma atomic emission spectroscopy (ICP-AES)

The analysis of leached metal ions from the samples was performed using the ICPE-9000 (Shimadzu, Tokyo, Japan). This analytical method was used to measure the quantity of leached metal ions present in the culture medium utilized for the 3 day cell seeding test. The ions released into the medium were quantified with a detection limit of 1 μg/mL.

2.7. Statistical analysis

For the comparison of cell viability for each element, one-way analysis of variance (ANOVA) followed by Tukey's multiple comparison tests was used. Pearson's correlation and single regression analyses were used to establish the significant determinants of cell viability. Single regression analysis was performed using IC_{50} and a newly defined compatibility coefficient, respectively. $P < 0.05$ was considered statistically significant.

3. Results

3.1. Electrochemical properties in biological culture medium

To elucidate the solubility of metals in a biological environment, their electrochemical properties were evaluated using potentiodynamic polarization in a serum-containing cell-culture medium maintained at 37 °C. Fig. 1 presents representative potentiodynamic polarization curves for each metal. The electrochemical kinetic parameters, corrosion potential (E_{corr}), corrosion current density (I_{corr}), cathodic Tafel slope (β_c), and anodic Tafel slope (β_a), were determined from these curves using the linear Tafel extrapolation method. The results are summarized in Table 1. The corrosion current density (I_{corr}) serves as an indicator of the dissolution rate of each metal, with higher values indicating faster ion release. Metals such as zinc (1566.0 nA • cm^{-2}), iron (1378.8 nA • cm^{-2}), and cobalt (908.7 nA • cm^{-2}) exhibited markedly elevated I_{corr} , indicating high corrosion activity. In contrast, several metals, including zirconium, titanium, and chromium exhibited exceptionally low I_{corr} , reflecting superior corrosion resistance.

Similarly, the anodic Tafel slopes (β_a) reflect passivation behavior. Metals such as hafnium (327 mV·dec^{-1}), titanium (310 mV·dec^{-1}), and niobium (312 mV·dec^{-1}) demonstrated high β_a values, indicative of stable passive oxide film formation. In contrast, zinc (70 mV·dec^{-1}) and iron (91 mV·dec^{-1}) exhibited low β_a values, suggesting limited passivation and greater susceptibility to dissolution. The observed differences in corrosion behavior may significantly influence cytocompatibility, emphasizing the importance of electrochemical assessment in materials design.

3.2. Evaluation of pure metal toxicity on osteoblast viability

The cytotoxicity of various metals toward osteoblasts was evaluated by quantifying cell survival on different metallic substrates (Fig. 2). Cell counts on titanium substrates after 1 day of incubation were normalized to 100%, serving as the reference for calculating relative cell viability on other metals. After 1day, significant reductions in cell counts were observed on silver, copper, cobalt, zinc, iron, and vanadium substrates compared with those on titanium. Specifically, survival rates for copper, cobalt, and zinc decreased to below 50% of those observed on titanium, and to below 25% for iron and vanadium. These reductions became more pronounced over time, with most of these metals exhibiting cell viability below 10% by day 7. In contrast, titanium, niobium, and aluminum maintained consistently high cell viability throughout the culture period, showing no significant changes at any time point. Intermediate behavior was observed for chromium, molybdenum, nickel, and tungsten, which exhibited gradual declines in viability over 7 days but did not reach the low levels observed for Fe and V. Consistent with these quantitative results, fluorescence microscopy images taken on day 3 (Fig. 3) revealed well-spread osteoblasts on cytocompatible metals such as Ti and Nb, whereas cells on Cu and V substrates appeared sparse and rounded. Cytotoxicity tests performed using an L929 fibroblast cell line showed trends consistent with those observed for osteoblasts (Supplementary Fig. 1). Specifically, metals such as Cu, Co, Fe, and V exhibited marked reductions in cell viability, whereas Ti, Nb, and Al sustained high cell survival throughout the culture period (Supplementary Fig. 2).

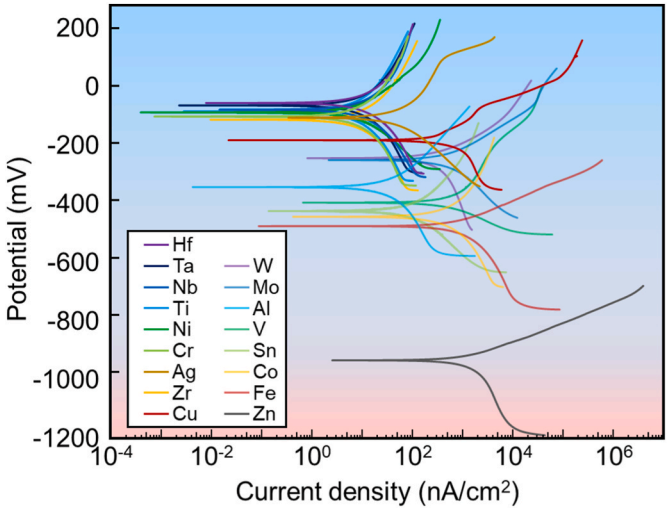

Fig. 1. Potentiodynamic polarization curves of pure metals in serum-containing medium. Potentiodynamic polarization curves for 17 pure metals were obtained in αMEM supplemented with serum at 37 °C using a three-electrode cell (Ag/AgCl reference, Pt counter electrode). The x-axis shows current density (nA • cm^{-2} logarithmic scale), and the y-axis shows potential (mV vs Ag/AgCl). Curves shown are representative of five independent measurements (n = 5).

3.3. Analysis of metal ion release from substrates

Metal ions released from the substrates after three days of incubation were quantified using the ICPE-9000 (Table 2). Aluminum, niobium, and titanium exhibited minimal ion release, with concentrations at or below 0.002 mg mL^{-1}. In contrast, iron, zinc, and cobalt exhibited relatively high solubility, with concentrations ranging from 0.657 to 0.910 mg mL^{-1}. Other metals, including copper, molybdenum, and tungsten, showed moderate ion-release levels, whereas vanadium exhibited lower yet detectable concentrations. These results generally correspond to the electrochemical corrosion behavior described in Section 3.1, reflecting differences in dissolution tendencies among the tested metals. Although potentiodynamic polarization measurements provide instantaneous corrosion current densities, these values represent steady-state dissolution rates. Through Faraday's law, the time-integrated corrosion current can be directly related to the cumulative amount of ions released over the immersion period.

4. Discussion

The development of metallic biomaterials has been supported by extensive prior work on biocompatibility and cytocompatibility, and numerous pioneering studies have elucidated the biological responses to metallic ions *in vivo* and *in vitro*. Nevertheless, there remains a lack of an element-level, quantitatively defined metric that directly links ion-release kinetics with ion-specific cytotoxicity under physiological conditions, which limits systematic screening of elemental compositions in alloy design. In this study, we established the Velocity–Ion Toxicity–Affinity (VITA) Index as a quantitatively defined and mechanistically informed framework for guiding the design and initial *in vitro* cytocompatibility screening of metallic biomaterials. The VITA Index integrates metal dissolution kinetics under physiological conditions ("Velocity") with the ion-specific cytotoxic thresholds ("Ion Toxicity") of the released species. The index exhibited a strong quantitative correlation with cell viability on metallic substrates, thereby validating its effectiveness as a rigorous and reproducible measure of *in vitro* cytocompatibility. Furthermore, by calculating VITA values for individual constituent elements and applying composition-weighted summation, we obtained first-order estimates of alloy cytocompatibility. Although this simplified approach does not explicitly incorporate synergistic effects in passive film formation, selective dissolution, or tribocorrosion, it nevertheless provided useful and consistent trends for established biomedical alloys. Therefore, the VITA Index serves as a practical element-level screening tool for alloy design, providing a quantitative foundation for early-stage exploration of multicomponent metallic systems, including AI-assisted and computational materials design.

Table 1
The electrochemical kinetic parameters of selected pure metals. This table presents the electrochemical corrosion data for a selection of metals, including corrosion potential (E_{corr}), corrosion current density (I_{corr}), cathodic Tafel slope (β_c), and anodic Tafel slope (β_a). The values are presented as mean ± standard deviation.

	I_{corr} $_{nA\cdot cm^{-2}}$	E_{corr} $_{mV}$	β_a $_{mV\cdot dec^{-1}}$	$-\beta_c$ $_{mV\cdot dec^{-1}}$
Ag	70.5 ± 11.2	−126 ± 20	139 ± 33	165 ± 43
Al	48.4 ± 14.6	−358 ± 92	285 ± 44	295 ± 49
Co	908.7 ± 246.5	−457 ± 80	127 ± 28	147 ± 47
Cu	612.8 ± 125.4	−201 ± 60	122 ± 29	163 ± 41
Mo	589.0 ± 71.4	−268 ± 44	143 ± 16	169 ± 43
Nb	17.9 ±2.7	−99 ± 18	312 ± 75	267 ± 39
Ti	12.0 ± 2.5	−104 ± 13	310 ± 56	298 ± 18
V	603.1 ± 73.1	−410 ± 129	163 ± 52	189 ± 22
W	351.3 ± 37.1	−262 ± 87	200 ± 18	148 ± 74
Zn	1566.0 ± 286.0	−938 ± 53	70 ± 12	199 ± 50
Cr	12.2 ± 6.1	−122 ± 40	277 ± 32	292 ± 49
Ni	10.4 ± 4.6	−108 ± 34	131 ± 21	152 ± 30
Fe	1378.8 ± 223.7	−489 ± 99	91 ± 29	149 ± 25
Sn	134.1 ± 23.0	−438 ± 86	150 ± 22	172 ± 48
Hf	19.7 ± 6.3	−77 ± 8	327 ± 70	283 ± 42
Ta	14.6 ± 3.3	−85 ± 11	285 ± 59	281 ± 67
Zr	11.2 ± 3.2	−133 ± 22	284 ± 37	235 ± 73

5. Electrochemical corrosion behavior in serum-containing physiological media

Electrochemical corrosion tests were performed in serum-containing αMEM supplemented with fetal bovine serum (FBS) to better approximate the physiological environment [10,24,25]. Corrosion current densities and Tafel slopes obtained in this medium aligned with trends for phosphate-buffered saline or Hanks' solutions, while highlighting the distinct influence of chloride ions in biological systems [26–30]. Niobium, titanium, chromium, nickel, hafnium, tantalum, and zirconium exhibited relatively low corrosion current densities, indicative of rapidly formed passive oxide layers. These passive oxides (such as TiO_2, Nb_2O_5, and HfO_2) exhibit high thermodynamic stability, semiconducting behavior, and self-healing capabilities, enhancing corrosion resistance in physiological conditions [27–29]. High anodic Tafel slopes ($\beta_a \geq 300$ mV dec^{-1}) further support strongly suppressed anodic reactions owing to the protective oxide layer.

In contrast, zinc and iron exhibited corrosion current densities approximately two orders of magnitude greater than those of passive metals such as titanium, niobium, or chromium, and displayed markedly negative corrosion potentials (E_{corr}). Zinc and iron possess limited capability to form stable passive films, leading to accelerated corrosion [31,32], and potential sacrificial-anode behavior when galvanically coupled with more noble metals, thereby necessitating careful consideration in the design of multi-metallic systems. Copper and cobalt, although exhibiting moderate corrosion current densities, formed oxide layers, Cu_2O/CuO and CoO/Co_3O_4 respectively, that are semiconducting or conductive and relatively thin [33,34]. These surface oxides lack the protective compactness and chemical resistance characteristic of those formed on passive metals, rendering them susceptible to chloride-induced degradation. This behavior is reflected in reduced anodic Tafel slopes and enhanced anodic dissolution. Notably, copper is susceptible to pitting corrosion under physiological conditions owing to localized surface film breakdown in the presence of Cl^- ions [35]. Passive metals such as titanium, chromium, niobium, and hafnium exhibited large β_c values, indicating suppressed cathodic activity owing to the passive oxide films, which reduce electron transfer at the interface.

The cathodic Tafel slope (β_c) reflects the overall cathodic reaction behavior at the metal–solution interface, which may involve oxygen reduction and/or other reduction processes depending on the environment. While β_c reflects overall cathodic reaction kinetics, it does not account for the contribution of reaction intermediates, such as reactive oxygen species (ROS), to cellular toxicity.

Collectively, these findings highlight the importance of corrosion current density as a principal determinant of electrochemical stability, while also recognizing the complementary roles of passive film properties and biological interactions in shaping overall corrosion behavior. The use of αMEM with FBS provides a platform that better approximates physiological environments than conventional salt solutions, yielding valuable insights into the electrochemical performance of candidate biomaterials under simulated physiological conditions.

6. Determinants of cell viability on metallic substrates

Cell viability on metallic substrates varied substantially depending on the type of metal. The behavior of cells adhered to metal is influenced by chemical effects arising from dissolved metal ions, biochemical effects from protein adsorption onto the substrate surface, physical effects due to adhesion-site loss induced by substrate corrosion, and mechanical effects resulting from changes in substrate stiffness [36–40]. Dissolved metal ions exert both beneficial and detrimental effects on cells, with high concentrations being cytotoxic [41,42]. For example, metals such as vanadium, iron, and copper promote reactive oxygen species (ROS) generation by catalyzing the Fenton reaction, thereby damaging cellular structures and DNA [43]. In contrast, titanium ions are generally considered less reactive under physiological conditions and less likely to

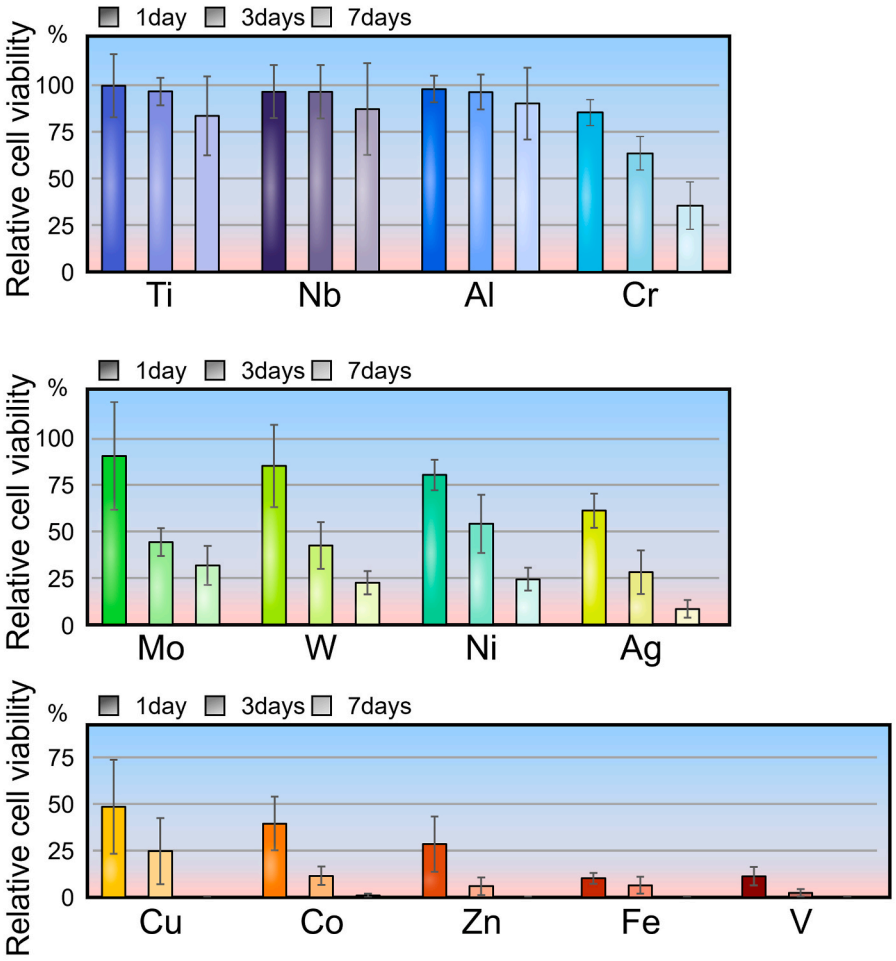

Fig. 2. Evaluation of pure metal toxicity on osteoblast viability. The toxicity of various metals on osteoblasts was evaluated by measuring the relative cell viability on different metal substrates over 1, 3, and 7 days. The results were normalized to the cell count on Ti substrates after 1 day, and were expressed as percentages. Error bars indicate standard deviation (n = 5).

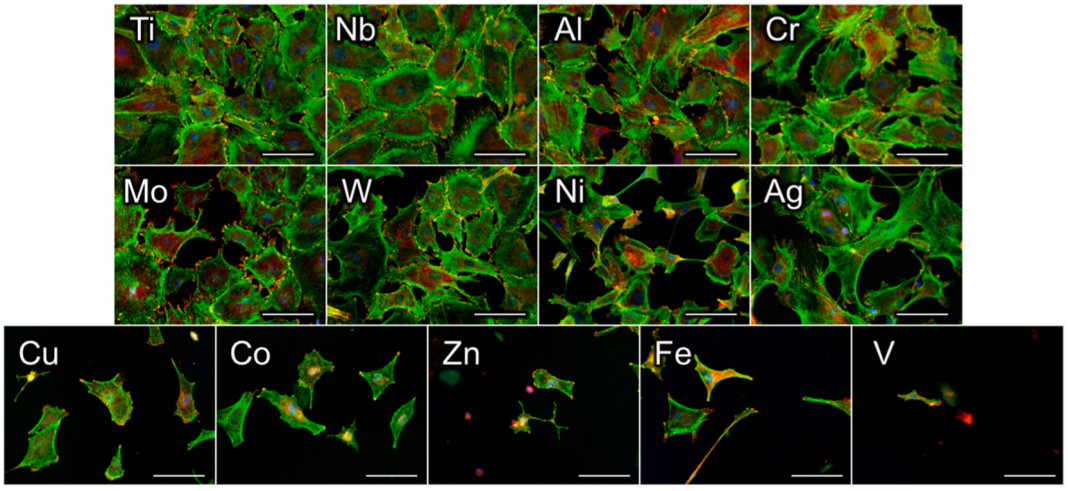

Fig. 3. Morphology of osteoblasts cultured on pure-metal substrates. Representative fluorescence images of osteoblasts after 3 days of culture on pure-metal substrates. Cells were stained for F-actin (green), nuclei (blue), and vinculin (red). Osteoblasts exhibited extensive spreading and well-organized actin filaments with focal adhesions on Ti, Nb, Al, Cr, Mo, and W substrates. On Ni and Ag, cell spreading was reduced, showing smaller cell areas. On Cu and Co, both the number and size of adherent cells were markedly diminished. On Zn, Fe, and V, only minimal adhesion was observed, with few or no spread cells detectable. Scale bars, 100 μm. (For interpretation of the references to colour in this figure legend, the reader is referred to the Web version of this article.)

induce harmful reactions compared with transition-metal ions. The observed decrease in cell numbers over time for most elements is likely

Table 2
The concentration of leached metal ions from selected pure metals. Metal ions eluted from the substrates after three days of incubation were detected using the ICPE-9000. The values are presented as mean ± standard deviation (n = 3).

Materials	The concentration of leached metal ions (mg·mL^{-1})
Aluminum (Al)	0.002 ± 0.000
Cobalt (Co)	0.657 ± 0.071
Copper (Cu)	0.530 ± 0.056
Iron (Fe)	0.910 ± 0.339
Molybdenum (Mo)	0.530 ± 0.040
Niobium (Nb)	0.001 ± 0.001
Titanium (Ti)	0.001 ± 0.001
Vanadium (V)	0.137 ± 0.015
Tungsten (W)	0.413 ± 0.169
Zinc (Zn)	0.747 ± 0.029

attributable to increasing concentrations of dissolved metal ions, indicating their predominant influence. To examine whether the observed cytotoxicity trends depend on cell type, relative cell viability obtained from fibroblast (L929) assays was directly compared with that from osteoblast assays for each metal (Supplementary Fig. 3). The resulting correlation plot revealed a strong linear relationship (R^2 = 0.905), demonstrating that cytotoxic responses are highly consistent between these two distinct cell types. This strong agreement indicates that the time-dependent decrease in cell numbers observed for most metals is predominantly governed by ion-release–driven effects, rather than by cell-type–specific sensitivity. In other words, the elemental cytotoxicity trends identified in the present study are largely preserved at the cell level across different cellular models. A slight systematic deviation was observed, with fibroblast viability tending to be marginally higher than that of osteoblasts. This difference may reflect intrinsic characteristics of immortalized cell lines, which are generally more tolerant to cytotoxic stress than primary cells. Nevertheless, this minor deviation does not affect the overall conclusion that the present evaluation captures broadly generalizable cytotoxic behavior.

The present study evaluates cytocompatibility under controlled *in vitro* conditions and is primarily intended to address early-stage material screening rather than *in vivo* biocompatibility. While this approach enables systematic comparison across elements and alloys, several limitations should be considered when interpreting the relevance of the VITA Index to *in vivo* scenarios.

First, cytocompatibility was assessed using a single osteoblast-based model under static culture conditions. Biological responses to metallic ions are known to vary across cell types, and future studies should therefore include additional cell lines, particularly those derived from nerve or muscle tissues that exhibit differing sensitivities to metal ions. Moreover, physiological environments are characterized by dynamic fluid flow and spatially heterogeneous chemical conditions, which may influence both corrosion behavior and cellular responses. Incorporation of flow-based bioreactor systems would allow closer approximation of such *in vivo* transport processes. In addition, the present investigation was limited to short-term exposure (up to 7 days). Prolonged metal-ion release over longer time scales may exacerbate surface degradation and structural defects arising from metal dissolution, potentially accelerating corrosion rates and altering local ion concentrations. Long-term studies are therefore necessary to assess the cumulative effects of chronic ion exposure on cytocompatibility.

Furthermore, the present framework does not explicitly consider cytotoxic effects mediated by reaction intermediates generated under *in vivo* conditions, such as reactive oxygen species (ROS) arising from inflammatory responses or mechanically assisted corrosion. These species can contribute to cellular damage independently of bulk ion concentrations, and incorporation of ROS-related descriptors represents an important direction for future refinement of the VITA framework.

It should also be noted that several degradation mechanisms relevant to *in vivo* implant performance—including galvanic coupling between alloy constituents, tribocorrosion, fretting, and mechanically assisted degradation—are not captured in the present experimental design. These phenomena play central roles in established *in vivo* biocompatibility frameworks but lie beyond the scope of the current study. Extensive experimental and conceptual frameworks for evaluating *in vivo* biocompatibility of metallic materials have been developed through seminal work by researchers such as Williams, Merritt, and Brown [13–16]. The present study does not seek to replace these established approaches. Rather, the VITA Index is positioned as a complementary, early-stage *in vitro* metric that integrates corrosion-driven ion release and ion-specific cytotoxicity to support materials selection at the elemental and compositional levels.

7. Corrosion current density as a quantitative proxy for metal-ion release

To clarify the relationship between metal-ion release observed in cell culture and the quantities of ions estimated from corrosion currents obtained in electrochemical tests, correlation coefficients were determined (Fig. 4). The inductively coupled plasma (ICP) measurements (Table 2) were normalized by the valence of each metal [20,44] (Supplementary Table 1) to determine the concentrations of dissolved metal ions. Correlation analysis yielded an R^2 value of 0.848 and a *p*-value of 0.00015, demonstrating a strong and statistically significant correlation between metal-ion release in cell culture and metal ion amount calculated from electrochemical corrosion currents. This finding suggests that corrosion current density in cell-culture medium can serve as a reliable proxy for metal-ion release. Accordingly, corrosion current density constitutes a valid quantitative estimator of ion release under *in vitro* conditions.

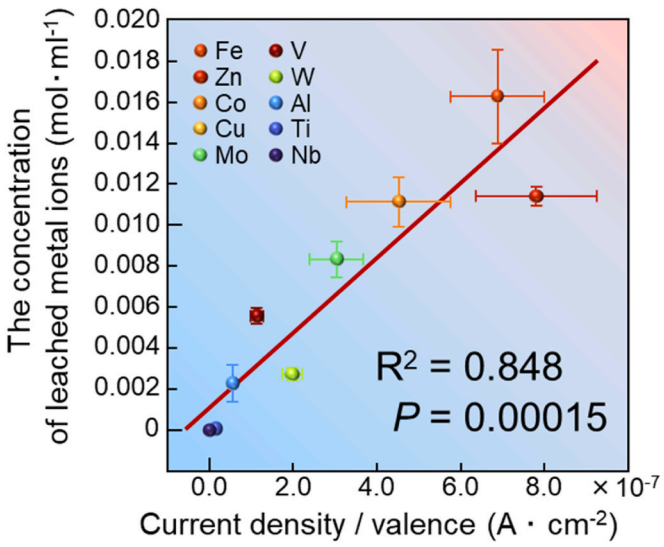

Fig. 4. Correlation between current density and leached metal ion concentration. Concentration of metal ions leached after 3 days of incubation in αMEM supplemented with serum, plotted against corrosion current density divided by valence as determined by potentiodynamic polarization testing. A strong linear correlation (R^2 = 0.848, p = 0.00015) demonstrates that electrochemical current density is a reliable predictor of ion release. Error bars indicate standard deviation.

8. Insufficiency of ion-specific toxicity metrics without corrosion kinetics

Metal-ion toxicity has traditionally been evaluated using metal salts, with IC_{50} values denoting the metal-ion concentrations that reduce cell viability by 50% [20] (Table 3 and Fig. 5). Higher IC_{50} values indicate lower intrinsic toxicity and, consequently, higher *in vitro* cytocompatibility. If differences in corrosion behavior are neglected, assuming a constant ion-release concentration for all metals, the Hill equation describing cell viability can be linearized within the central response range via a first-order Taylor expansion, yielding a proportional relationship between cell viability and ion concentration (full derivation provided in the Supplementary Note). Under this assumption, a semi-logarithmic plot is expected to yield a linear relationship. However, the correlation between IC_{50i} values and cellular viability was weak ($R^2 = 0.344$, $p = 0.0353$) (Fig. 5 and Supplementary Fig. 4). In practice, corrosion-rate–dependent ion release varies markedly among metals; therefore, IC_{50} alone is insufficient to describe *in vitro* cytocompatibility. For instance, despite possessing a high IC_{50} value, zirconium exhibited low effective toxicity due to its minimal dissolution in the culture medium.

It should be noted that the IC50 values primarily reflect ion-related cytotoxicity; however, strictly speaking, they do not represent the toxicity of idealized free metal ions alone. Under physiological culture conditions, metal species introduced as salts can undergo hydration, hydrolysis, complexation with medium components, and, in some cases, precipitation or colloid formation. Consequently, IC50 values should be interpreted as an empirical measure of the effective cytotoxicity arising from metal-related species present after dissolution, rather than from free ions in isolation.

As a representative example, titanium exhibits extremely low apparent ionic solubility under neutral physiological pH owing to rapid hydrolysis and the formation of insoluble or colloidal oxide/hydroxide phases. As a result, the effective concentration of freely hydrated Ti ions is expected to be very low, which can substantially reduce ionic bioavailability in solution. While such solubility and speciation effects are not explicitly modeled in the present framework, their net biological impact is effectively incorporated into the IC50 parameter. This limitation also represents an important direction for future refinement, where incorporating speciation-aware descriptors may further improve interpretability and predictive accuracy. Nevertheless, despite capturing effective ion-related cytotoxicity, IC50-based descriptors alone exhibited only a weak correlation with cellular viability when applied to bulk metallic materials.

In contrast, corrosion current density, which reflects ion release, exhibited a strong correlation with cell viability, underscoring the necessity of accounting for metal corrosion behavior ($R^2 = 0.785$, $p = 0.000561$) (Supplementary Fig. 5). However, chromium, nickel, and silver displayed low cell viability despite low corrosion current densities, owing to the exclusion of ion-specific toxicity from this metric. This limited correlation indicates that, for solid metals, cytocompatibility is not governed solely by the intrinsic toxicity of dissolved species, but is strongly modulated by corrosion behavior that controls the rate and extent of ion release from the material surface. In other words, even metals associated with relatively high effective ionic toxicity may exhibit favorable biological responses when corrosion rates are sufficiently low, whereas metals with moderate intrinsic toxicity can induce pronounced cytotoxic effects if corrosion-driven ion release is significant. These observations reinforce the central premise that corrosion kinetics constitute a critical determinant of cytocompatibility for bulk metallic biomaterials, and that meaningful assessment requires explicit consideration of both ion-specific toxicity and corrosion-controlled ion release.

Table 3
Comparison of IC_{50} and Velocity–Ion Toxicity–Affinity (VITA) Index for predicting cell viability. IC_{50} values for metal ions were obtained from previously reported cytotoxicity data [20]. VITA values were calculated in this study. IC_{50} values are presented in $mol.L^{-1}$ and VITA values are dimensionless.

Materials	IC_{50} ($mol \cdot L^{-1}$)	VITA Index Velocity–Ion Toxicity–Affinity
Silver (Ag)	2.77×10^{-6}	1.02×10^{-2}
Aluminum (Al)	2.92×10^{-3}	4.69×10^{1}
Cobalt (Co)	1.12×10^{-5}	6.39×10^{-3}
Chromium (Cr)	1.27×10^{-5}	8.12×10^{-1}
Copper (Cu)	1.59×10^{-5}	1.34×10^{-2}
Iron (Fe)	5.83×10^{-4}	2.19×10^{-1}
Hafnium (Hf)	9.33×10^{-4}	4.91×10^{1}
Molybdenum (Mo)	3.52×10^{-3}	7.74×10^{0}
Niobium (Nb)	1.47×10^{-3}	1.06×10^{2}
Nickel (Ni)	5.22×10^{-5}	2.60×10^{0}
Tin (Sn)	2.50×10^{-5}	9.66×10^{-2}
Tantalum (Ta)	2.06×10^{-3}	1.83×10^{2}
Titanium (Ti)	8.71×10^{-4}	7.52×10^{1}
Vanadium (V)	2.25×10^{-6}	2.90×10^{-3}
Tungsten (W)	3.20×10^{-4}	1.42×10^{0}
Zinc (Zn)	9.00×10^{-5}	2.98×10^{-2}
Zirconium (Zr)	2.83×10^{-3}	2.61×10^{2}

9. Definition of the Velocity–Ion Toxicity–Affinity (VITA) Index

Accordingly, we propose a novel index, the Velocity–Ion Toxicity–Affinity (VITA) Index, defined by the following equation:

$$VITA_i = \frac{IC_{50i} \cdot Z_i}{S \cdot I_{corri}} \tag{1}$$

Here, for element *i*, $VITA_i$ denotes its VITA value; IC_{50i} denotes its IC_{50} value; Z_i denotes its valence; and I_{corri} denotes its corrosion current density; and S $\left(= 3860\ mol \cdot cm^2 \cdot s \cdot C^{-1} \cdot L^{-1}\right)$ denotes a scaling factor introduced to normalize the index and render it dimensionless. This equation represents the ratio of the allowable ion concentration (IC_{50i}) to the ion-release rate, thereby quantifying the affinity of the metal for cellular systems. The relationship between cell survival v and ion concentration C is generally expressed by the Hill equation:

$$v = \frac{1}{1 + \left(\frac{C}{IC_{50i}}\right)^n} \tag{2}$$

Here, v denotes the cell viability, C denotes the ion release concentration, and n denotes the Hill coefficient. Moreover, our results demonstrated that C is proportional to the corrosion current density normalized by valence. Using the previously defined $VITA_i$ Eq. (1), this relationship can be rewritten as:

$$C = S.\frac{I_{corri}}{Z_i} = \frac{IC_{50i}}{VITA_i} \tag{3}$$

Substituting into the Hill equation Eq. (2) yields:

$$v = \frac{1}{1 + \left(\frac{1}{VITA_i}\right)^n} \tag{4}$$

This equation indicates that the ratio of toxicity threshold to corrosion rate directly determines cell survival, thereby forming the physical basis of the VITA Index concept.

This proportionality between ion concentration and corrosion current density is not merely empirical but can be derived directly from

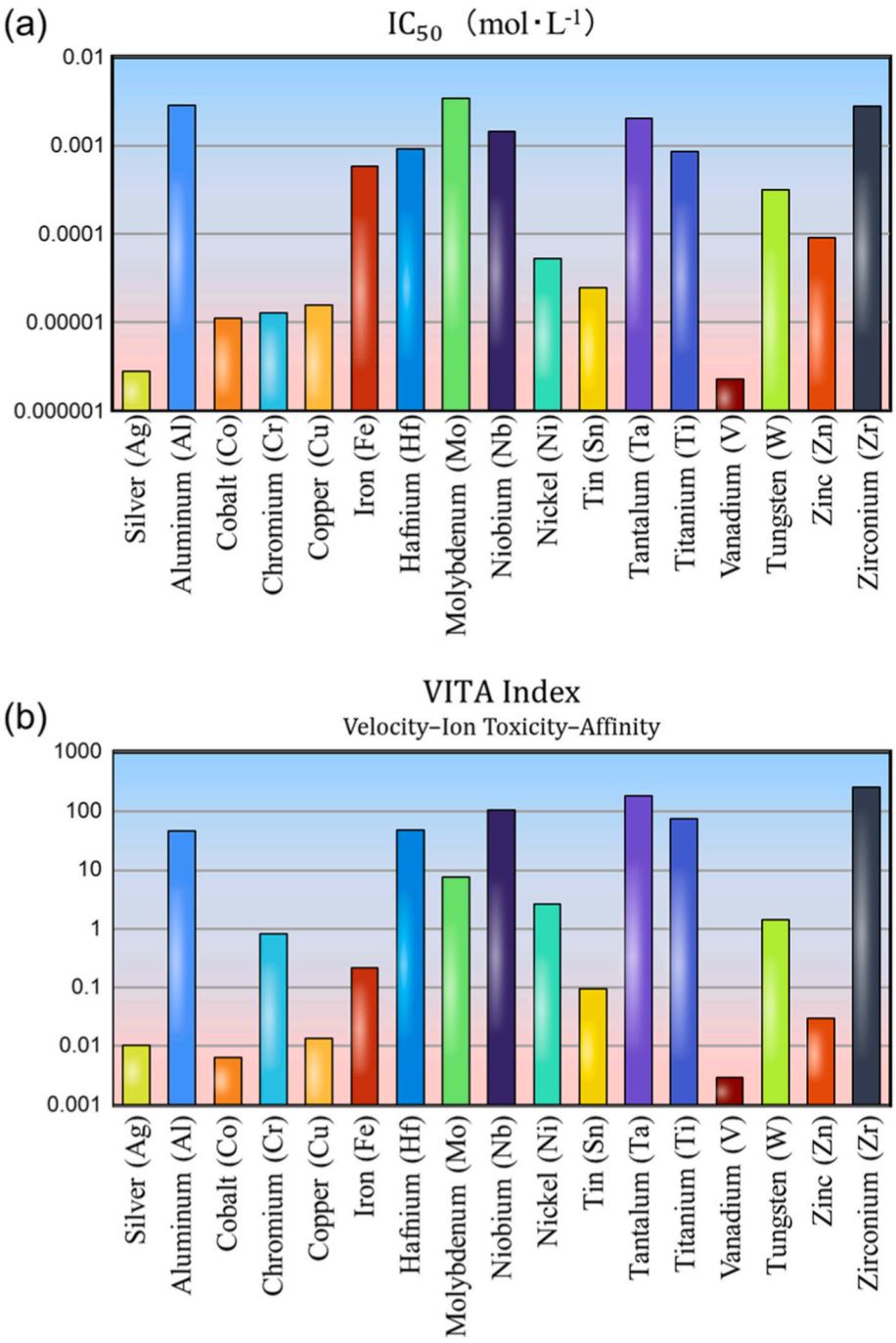

Fig. 5. Comparison of the IC50 values and VITA values. Bar charts showing the IC50 values and corresponding VITA values summarized in Table 3. In particular, Cr, Mo, Fe, Ni, W, and Zn showed large discrepancies between IC50 and VITA.

Faraday's law of electrochemical dissolution. This fundamental electrochemical law quantitatively relates the total electric charge passed to the amount of material dissolved, thereby establishing a physical correspondence between current density and the amount of ions released into the medium:

$$C = \frac{A \cdot t}{F \cdot V} \cdot \frac{I_{corr\,i}}{Z_i} \tag{5}$$

Here, A denotes the exposed surface area, t denotes the exposure time, F denotes the Faraday constant ($= 96485\ \mathrm{C \cdot mol^{-1}}$), and V denotes the volume of the medium. From this relationship, the scaling factor S can be expressed as:

$$S = \frac{A \cdot t}{F \cdot V} \tag{6}$$

In this definition, S is a physically meaningful scaling factor determined entirely by the test geometry and exposure parameters through Faraday's law, rather than an empirical fitting constant. Within this formulation, the difference in time scales between instantaneous electrochemical measurements and time-integrated ion concentrations measured by ICP is explicitly accounted for through a scaling factor derived from Faraday's law, enabling direct comparison between corrosion current density and cumulative ion release under identical *in vitro* conditions. The value of S derived from this study was $3860\ \mathrm{mol \cdot cm^2 \cdot s \cdot C^{-1} \cdot L^{-1}}$, which is on the same numerical scale as the

value ($\sim 5000\ \mathrm{mol{\cdot}cm^2{\cdot}s{\cdot}C^{-1}{\cdot}L^{-1}}$) calculated from the experimental conditions ($A = 2\ \mathrm{cm^2}$, $V = 1\ \mathrm{mL}$, $t = 3$ days ($= 259{,}200$ s)). The close agreement between its theoretical value and the experimentally obtained value confirms that the VITA Index is not merely empirical, but is grounded in a physically consistent description of ion release and ion toxicity.

To assess whether the VITA Index serves as a reliable predictor of cytocompatibility, we examined the relationship between $VITA_i$ and measured cell viability. Plotting $VITA_i$ against cell viability revealed a strong positive correlation ($R^2 = 0.814$, $p = 0.000025$), demonstrating that the VITA Index effectively predicts metal cytocompatibility (Fig. 6b and Supplementary Fig. 6). While the correlation obtained using the VITA Index is strong ($R^2 \approx 0.8$), the remaining unexplained variance is likely attributable to biological factors not explicitly included in this first-order framework, such as protein adsorption behavior, time-dependent evolution of surface chemistry, and cell-type–specific stress responses. Using $\log_{10} VITA_i$ as the variable, the regression equation is:

$$v = 0.20 \log_{10} VITA_i + 0.50 \tag{7}$$

Importantly, this linear relationship is not merely an empirical fit but can be physically interpreted as a first-order Taylor approximation of the Hill equation with $VITA_i$ Eq. (4) in the central response region. Under this approximation, cell viability can be described as a logistic function of $\log_{10} VITA_i$ and thus justifies the linear regression in $\log_{10} VITA_i$ shown in Eq. (7), interpreting the slope as proportional to the effective Hill coefficient. A full derivation is provided in the Supplementary Note.

10. Validation of the VITA Index for predicting alloy cytocompatibility

This regression equation, derived from pure-metal data, can be extended to alloys under an idealized first-order model in which each constituent element dissolves independently. Under this assumption, the VITA value of an alloy, $VITA_{alloy}$ is defined as the atomic-fraction-weighted sum of the VITA values of its constituent elements:

$$VITA_{alloy} = \sum_i x_i \cdot VITA_i \tag{8}$$

$$\begin{aligned} v &= 0.20 \log_{10} VITA_{alloy} + 0.50 \pm 1.96 \times \sqrt{MSE} \\ &= 0.20 \log_{10} VITA_{alloy} + 0.50 \pm 0.129 \end{aligned} \tag{9}$$

Here, x_i denotes the atomic fraction of element i. To evaluate the applicability of the proposed index to alloys, the resulting alloy VITA value was substituted into Eq. (7) to predict *in vitro* cell survival. The predictive accuracy of the VITA Index was then compared with that of conventional indices (IC_{50} and corrosion current density) for representative metallic alloys used in biomaterials (SUS-316L) as well as recently developed bio high-entropy alloys (BioHEAs) designed for *in vitro* biological evaluation (Fig. 7). Each predictive index was calculated as a linear combination of the constituent elements, weighted according to their atomic fractions. For each predictive index, predicted values were obtained from the regression equations in Supplementary Table 2 and compared with the observed values in the referenced literature [5,6,17–19,45]. A quantitative comparison based on the mean squared error (MSE) showed that the VITA Index exhibited the lowest prediction error among the tested metrics, indicating superior accuracy in predicting alloy cytocompatibility trend (Table 4, Supplementary Table 3 and Supplementary Table 4). The 95% prediction error was approximated as $\pm 1.96 \times \sqrt{MSE}$ based on the residual variability of each index.

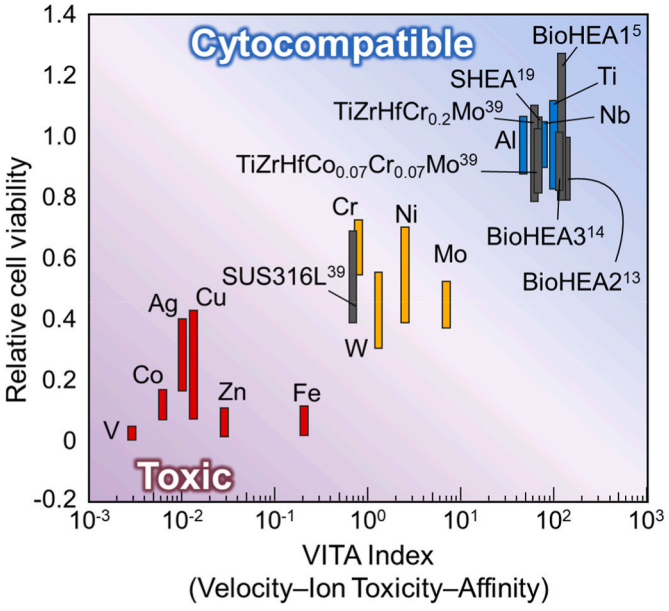

Fig. 7. Alloy cytocompatibility prediction using the Velocity–Ion Toxicity–Affinity (VITA) Index.

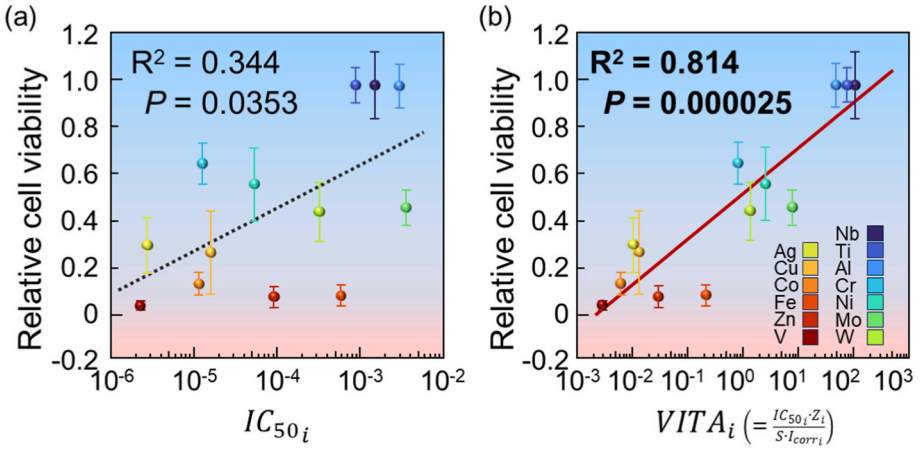

Fig. 6. Comparison of IC_{50} and VITA Index in predicting cell viability. The graph shows the horizontal axis converted to a logarithmic scale. (a) Correlation between IC_{50i} values and relative cell viability of osteoblasts cultured on pure metals. The correlation was weak ($R^2 = 0.344$, $p = 0.0353$). (b) Correlation between $VITA_i$ calculated and relative cell viability. A strong correlation was observed ($R^2 = 0.814$, $p = 0.000025$), supporting VITA Index as a better predictor of cytocompatibility compared to IC_{50} alone. Error bars represent standard deviation (n = 5).

Table 4
Comparison of predictive accuracy among VITA, IC_{50}, and corrosion current density for biomedical alloys. Mean squared error (MSE) was calculated by comparing predicted cell viability values for biomedical alloys, derived from regression equations in Fig. 6 and Supplementary Fig. 6. VITA showed the lowest MSE (0.00435), indicating superior predictive performance compared to IC_{50} (0.0606) and corrosion current density (0.0226). The 95% prediction error was approximated as $\pm 1.96 \times \sqrt{MSE}$ based on the residual variability of each index.

Predictive index	VITA Index	IC_{50}	Corrosion current density
MSE	0.00435	0.0606	0.0226
95% *prediction interval* ($\pm 1.96 \times \sqrt{MSE}$)	0.129	0.483	0.294

11. Implications of the VITA Index for cytocompatibility design of high-entropy alloys

The global demand for biomedical alloys is increasing, with particular attention directed toward high-entropy alloys (HEAs) owing to their exceptional design flexibility. HEAs constitute a novel class of materials recognized for their potential in biomedical applications, owing to their high strength, ductility, and resistance to wear and corrosion [46–48]. Key design parameters for HEAs include the enthalpy of mixing (ΔH), the configurational entropy (Ω), the atomic size difference (δ), and the valence electron concentration [49–52]. These parameters are critical for achieving stable single-phase solid solutions, thereby optimizing the mechanical and chemical properties of HEAs. Despite significant progress in HEA design, their cytocompatibility remains insufficiently investigated. The VITA Index developed in this study accurately predicted the cytocompatibility of HEAs. Integrating the VITA Index with conventional HEA design parameters is expected to enhance predictive accuracy and broaden the range of element selection for biomedical applications, and can be readily incorporated into computational design frameworks for multi-principal element alloys, such as AI-driven alloy design and high-throughput screening.

12. Limitation

This approach assumes an idealized first-order model in which the alloy surface possesses a uniform composition and that each constituent metal corrodes independently and in direct proportion to its composition ratio. While this simplification facilitates practical prediction, it does not account for complex metallurgical phenomena such as selective dissolution, galvanic coupling, or microstructural heterogeneity that may occur in certain alloy systems [53]. Interactions among alloying elements can give rise to localized corrosion behavior or surface phase separation, potentially causing deviations from this linear summation model in the present formulation.

The relationship between VITA values and relative cell viability is shown for pure metals (red, yellow, blue) and biomedical alloys (grey), including SUS316L stainless steel, TiZrHf-based HEAs, and BioHEAs (BioHEA1–3). The detailed alloy compositions are: BioHEA1 (TiNbTaZrMoHf), BioHEA2 ($Ti_{1.4}Zr_{1.4}Nb_{0.6}Ta_{0.6}Mo_{0.6}$), BioHEA3 ($Ti_{28.33}Zr_{28.33}Hf_{28.33}Nb_{6.74}Ta_{6.74}Mo_{1.55}$). The center of each bar represents the mean value, and the vertical length indicates the standard deviation (SD) ($n = 5$). The x-axis is plotted on a logarithmic scale, and the background gradient illustrates the transition from toxic (low VITA) to biocompatible (high VITA) materials.

Beyond these limitations, it is also important to recognize that corrosion resistance of biomedical alloys is intrinsically linked to the formation and stability of passive surface films. The development, composition, and repairability of such films are governed by synergistic interactions among alloying elements and are strongly influenced by environmental and electrochemical conditions. These passivation-related effects cannot be fully captured by a linear, composition-based approximation alone.

For example, while iron exhibits a relatively low VITA value when evaluated as a single-element material, iron-based alloys such as 316L stainless steel demonstrate excellent corrosion resistance and have been successfully used as biomedical materials for decades. This apparent discrepancy arises because, in alloys such as 316L, iron is effectively protected by the formation of Cr-rich passive oxide films.

To clarify this point and to assist in the interpretation of the present results, we provide an extended discussion in the Supplementary Note that examines passive film formation from thermodynamic, electrochemical, and geometric perspectives, including oxide stability, Pourbaix (pH–potential) considerations, oxide solubility, and Pilling–Bedworth ratio. These considerations are not incorporated into the present index formulation but are discussed to define the appropriate scope, limitations, and potential future development of the VITA Index.

More broadly, *in vivo* biocompatibility is not dictated by ion-mediated cytotoxicity alone, but also by the local tissue microenvironment and the host response to the implant, including protein adsorption, inflammation/foreign body reaction, mechanical loading, and tissue-specific remodeling processes [54–57]. In bone applications in particular, long-term implant success depends strongly on osseointegration phenomena occurring across hierarchical length scales at the bone–implant interface and on the implant's geometry and surface architecture. Porous or lattice-like three-dimensional architectures that approximate native trabecular microstructure can facilitate bone ingrowth and vascularization, while anisotropic micro/nanotopographic cues can guide cell orientation (contact guidance) and subsequent extracellular matrix organization. These environment- and structure-dependent determinants of tissue integration are outside the scope of the present VITA Index, which is intentionally formulated as a first-order predictor centered on ion release and ion-specific toxicity.

Nevertheless, the cytocompatibility predicted by the VITA Index closely matched the experimentally measured cell viability values and outperformed conventional indices, thereby indicating that the VITA Index provides a reliable first-order predictor of alloy cytocompatibility. This finding indicates that ion release and the resulting ion toxicity are primary determinants of cytocompatibility, underscoring the utility of the VITA Index, which is defined with a focus exclusively on its essential determinants—ion release rate and ion-specific toxicity—in a conceptually simple form.

13. Conclusion

This study established the Velocity–Ion Toxicity–Affinity (VITA) Index as a quantitative and mechanistically grounded metric for predicting *in vitro* cytocompatibility trends of biomedical alloys, including both conventional and multi-element alloys. The VITA Index integrates metal dissolution behavior under *in vitro* physiological-like conditions with the toxicity of the released ions, enabling a comprehensive assessment of cytocompatibility. Electrochemical measurements and cell-culture studies demonstrated a strong correlation between the VITA Index and cell viability, with first-order predictions closely matching experimental observations. These findings indicate that the VITA Index captures the primary determinants governing cytocompatibility—ion release and ion-specific toxicity—thereby underscoring its utility in early-stage alloy design.

Overall, the VITA Index provides a robust and versatile framework for the rational selection and early-stage screening of metallic alloys with improved *in vitro* cytocompatibility, translating materials science principles into practical tools for next-generation data-driven biomaterials development.

CRediT authorship contribution statement

Tadaaki Matsuzaka: Writing – original draft, Visualization, Methodology, Investigation, Formal analysis. **Aira Matsugaki:** Writing – review & editing, Supervision, Methodology, Funding acquisition, Formal analysis. **Takayoshi Nakano:** Writing – review & editing, Supervision, Project administration, Funding acquisition, Conceptualization.

Ethics approval

The study protocol was approved by the University of Osaka Committee for Animal Experimentation (Approval No. 2020-1-0).

Declaration of competing interest

The authors declare that they have no known competing financial interests or personal relationships that could have appeared to influence the work reported in this paper.

Acknowledgements

This work was supported by a Grant-in-Aid for Scientific Research (KAKENHI) [Grant Number: 24H00382, 23H00235, 21H05197] from the Japan Society for the Promotion of Science (JSPS). This work was partially supported by the Core Research for Evolutional Science and Technology (CREST) [Grant Numbers: JPMJCR2194 and JPMJCR22L5] and the Fusion Oriented Research for Disruptive Science and Technology (FOREST) [Grant Number: JPMJFR234X] from the Japan Science and Technology Agency (JST).

Appendix A. Supplementary data

Supplementary data to this article can be found online at https://doi.org/10.1016/j.biomaterials.2026.124101.

Data availability

The datasets generated during and/or analyzed during the current study are available from the corresponding author upon request.

References

[1] T. Hanawa, Biocompatibility of titanium from the viewpoint of its surface, Sci. Technol. Adv. Mater. 23 (2022) 457–472, https://doi.org/10.1080/14686996.2022.2106156.
[2] S. Ali, A.M.A. Rani, Z. Baig, S.W. Ahmed, G. Hussain, K. Subramaniam, S. Hastuty, T.V.V.L.N. Rao, Biocompatibility and corrosion resistance of metallic biomaterials, Corrosion Rev. 38 (2020) 381–402, https://doi.org/10.1515/corrrev-2020-0001.
[3] H. Li, Z. Yao, J. Zhang, X. Cai, L. Li, G. Liu, J. Liu, L. Cui, J. Huang, The progress on physicochemical properties and biocompatibility of tantalum-based metal bone implants, SN Appl. Sci. 2 (2020) 671, https://doi.org/10.1007/s42452-020-2480-2.
[4] K. Yuan, C. Deng, L. Tan, X. Wang, W. Yan, X. Dai, R. Du, Y. Zheng, H. Zhang, G. Wang, Structural and temporal dynamics analysis of zinc-based biomaterials: history, research hotspots and emerging trends, Bioact. Mater. 35 (2024) 306–329, https://doi.org/10.1016/j.bioactmat.2024.01.017.
[5] M. Todai, T. Nagase, T. Hori, A. Matsugaki, A. Sekita, T. Nakano, Novel TiNbTaZrMo high-entropy alloys for metallic biomaterials, Scr. Mater. 129 (2017) 65–68, https://doi.org/10.1016/j.scriptamat.2016.10.028.
[6] Y. Iijima, T. Nagase, A. Matsugaki, P. Wang, K. Ameyama, T. Nakano, Design and development of Ti–Zr–Hf–Nb–Ta–Mo high-entropy alloys for metallic biomaterials, Mater. Des. 202 (2021) 109548, https://doi.org/10.1016/j.matdes.2021.109548.
[7] J. Kim, H. Pan, Effects of magnesium alloy corrosion on biological response – perspectives of metal-cell interaction, Prog. Mater. Sci. 133 (2023) 101039, https://doi.org/10.1016/j.pmatsci.2022.101039.
[8] P. Hou, P. Han, C. Zhao, H. Wu, J. Ni, S. Zhang, J. Liu, Y. Zhang, H. Xu, P. Cheng, S. Liu, Y. Zheng, X. Zhang, Y. Chai, Accelerating corrosion of pure magnesium Co-implanted with titanium in vivo, Sci. Rep. 7 (2017) 41924, https://doi.org/10.1038/srep41924.
[9] D. Xu, T. Gu, D.R. Lovley, Microbially mediated metal corrosion, Nat. Rev. Microbiol. 21 (2023) 705–718, https://doi.org/10.1038/s41579-023-00920-3.
[10] C. Liu, Y. Li, Q. Ge, Z. Liu, A. Qiao, Y. Mu, Mechanical characteristics and in vitro degradation of biodegradable Zn-Al alloy, Mater. Lett. 300 (2021) 130181, https://doi.org/10.1016/j.matlet.2021.130181.
[11] S. Almathami, J. Venezuela, N. Yang, Y. Wang, Z. Mardina, M. Dargusch, Exploring the influence of biologically relevant ions on the corrosion behavior of biodegradable zinc in physiological fluids, ACS Biomater. Sci. Eng. 9 (2023) 2301–2316, https://doi.org/10.1021/acsbiomaterials.2c00901.
[12] M.M. Alves, Interplay between zinc surface functionalization and degradation behavior in targeted implant applications, Surf. Interfaces 58 (2025) 105776, https://doi.org/10.1016/j.surfin.2025.105776.
[13] K. Merritt, S.A. Brown, N.A. Sharkey, Blood distribution of nickel, cobalt, and chromium following intramuscular injection into hamsters, J. Biomed. Mater. Res. 18 (1984) 991–1004, https://doi.org/10.1002/jbm.820180904.
[14] K. Merritt, S.A. Brown, Release of hexavalent chromium from corrosion of stainless steel and Cobalt—Chromium alloys, J. Biomed. Mater. Res. 29 (1995) 627–633, https://doi.org/10.1002/jbm.820290510.
[15] R.L. Williams, S.A. Brown, K. Merritt, Electrochemical studies on the influence of proteins on the corrosion of implant alloys, Biomaterials 9 (1988) 181–186, https://doi.org/10.1016/0142-9612(88)90119-6.
[16] D.F. Williams, On the mechanisms of biocompatibility, Biomaterials 29 (2008) 2941–2953, https://doi.org/10.1016/j.biomaterials.2008.04.023.
[17] T. Ishimoto, R. Ozasa, K. Nakano, M. Weinmann, C. Schnitter, M. Stenzel, A. Matsugaki, T. Nagase, T. Matsuzaka, M. Todai, H.S. Kim, T. Nakano, Development of TiNbTaZrMo bio-high entropy alloy (BioHEA) super-solid solution by selective laser melting, and its improved mechanical property and biocompatibility, Scr. Mater. 194 (2021) 113658, https://doi.org/10.1016/j.scriptamat.2020.113658.
[18] O. Gokcekaya, T. Ishimoto, Y. Nishikawa, Y.S. Kim, A. Matsugaki, R. Ozasa, M. Weinmann, C. Schnitter, M. Stenzel, H.S. Kim, Y. Miyabayashi, T. Nakano, Novel single crystalline-like non-equiatomic TiZrHfNbTaMo bio-high entropy alloy (BioHEA) developed by laser powder bed fusion, Mater. Res. Lett. 11 (2023) 274–280, https://doi.org/10.1080/21663831.2022.2147406.
[19] T. Matsuzaka, A. Hyakubu, Y.S. Kim, A. Matsugaki, T. Nagase, T. Ishimoto, R. Ozasa, H.S. Kim, T. Mizuguchi, O. Gokcekaya, T. Nakano, Development of an equiatomic octonary TiNbTaZrMoHfWCr super-high-entropy alloy for biomedical applications, Mater. Chem. Phys. 316 (2024) 129120, https://doi.org/10.1016/j.matchemphys.2024.129120.
[20] A. Yamamoto, R. Honma, M. Sumita, Cytotoxicity evaluation of 43 metal salts using murine fibroblasts and osteoblastic cells, J. Biomed. Mater. Res. 39 (1998) 331–340, https://doi.org/10.1002/(SICI)1097-4636(199802)39:2%253C331::AID-JBM22%253E3.0.CO;2-E.
[21] Y. Li, H. Jahr, K. Lietaert, P. Pavanram, A. Yilmaz, L.I. Fockaert, M.A. Leeflang, B. Pouran, Y. Gonzalez-Garcia, H. Weinans, J.M.C. Mol, J. Zhou, A.A. Zadpoor, Additively manufactured biodegradable porous iron, Acta Biomater. 77 (2018) 380–393, https://doi.org/10.1016/j.actbio.2018.07.011.
[22] R.P. Nogueira, J. Deuzimar Uchoa, F. Hilario, G. de F. Santana-Melo, L.M.R. de Vasconcellos, F.R. Marciano, V. Roche, A. Moreira Jorge Junior, A.O. Lobo, Characterization of optimized TiO2 nanotubes morphology for medical implants: biological activity and corrosion resistance, Int. J. Nanomedicine 16 (2021) 667–682, https://doi.org/10.2147/IJN.S285805.
[23] S. Javadi, L. Castro, R. Arrabal, E. Matykina, Metal ion release from PEO-coated Ti6Al4V DMLS alloy for orthopedic implants, J. Funct. Biomater. 16 (2025) 362, https://doi.org/10.3390/jfb16100362.
[24] N.S. Al-Mamun, K. Mairaj Deen, W. Haider, E. Asselin, I. Shabib, Corrosion behavior and biocompatibility of additively manufactured 316L stainless steel in a physiological environment: the effect of citrate ions, Addit. Manuf. 34 (2020) 101237, https://doi.org/10.1016/j.addma.2020.101237.
[25] X. Liu, H. Yang, Y. Liu, P. Xiong, H. Guo, H.-H. Huang, Y. Zheng, Comparative studies on degradation behavior of pure zinc in various simulated body fluids, JOM 71 (2019) 1414–1425, https://doi.org/10.1007/s11837-019-03357-3.
[26] M. Amirnejad, M. Rajabi, R. Jamaati, The effect of crystallographic texture as a distinct effective parameter on the biocorrosion performance of Ti6Al4V alloy in PBS solution, Corros. Sci. 179 (2021) 109100, https://doi.org/10.1016/j.corsci.2020.109100.
[27] D. Mei, S.V. Lamaka, X. Lu, M.L. Zheludkevich, Selecting medium for corrosion testing of bioabsorbable magnesium and other metals – a critical review, Corros. Sci. 171 (2020) 108722, https://doi.org/10.1016/j.corsci.2020.108722.
[28] K.-K. Wong, H.-C. Hsu, S.-C. Wu, T.-L. Hung, W.-F. Ho, Structure, properties, and corrosion behavior of Ti-Rich TiZrNbTa medium-entropy alloys with $\beta+\alpha''+\alpha'$ for biomedical application, Materials 15 (2022) 7953, https://doi.org/10.3390/ma15227953.
[29] A. Kumar, A. Choudhari, A.K. Gupta, A. Kumar, Rare-earth based magnesium alloys as a potential biomaterial for the future, J. Magnesium Alloys 12 (2024) 3841–3897, https://doi.org/10.1016/j.jma.2024.10.006.
[30] S. Hu, T. Li, X. Li, G. Zhang, J. Li, F. Guo, D. Liu, Electrochemical behavior, passive film characterization and in vitro biocompatibility of Ti–Zr–Nb medium-entropy alloys, J. Mater. Sci. 58 (2023) 946–960, https://doi.org/10.1007/s10853-022-08128-1.
[31] Y. Chen, W. Zhang, M.F. Maitz, M. Chen, H. Zhang, J. Mao, Y. Zhao, N. Huang, G. Wan, Comparative corrosion behavior of Zn with Fe and Mg in the course of immersion degradation in phosphate buffered saline, Corros. Sci. 111 (2016) 541–555, https://doi.org/10.1016/j.corsci.2016.05.039.
[32] Z. Huang, L. Zhang, T. Nie, G. Xu, Y. Zhao, J. Yang, J. Dai, Z. Huang, C. Guo, C. Wang, J. Bai, F. Xue, C. Chu, Corrosion behavior and hemocompatibility of a Cu (II)-incorporated polydopamine coating on biodegradable zinc, Prog. Org. Coating 203 (2025) 109178, https://doi.org/10.1016/j.porgcoat.2025.109178.

[33] Y. Zheng, T. Huang, J. Yao, G. Fargas, E. Armelin, L. Llanes, C. Xie, D. Crespo, P. Bruna, O. Lavigne, Electrochemical corrosion behavior of WC-Co and WC-Ni cemented carbides: effect of chloride and sulfate ions, Int. J. Refract. Metals Hard Mater. 132 (2025) 107224, https://doi.org/10.1016/j.ijrmhm.2025.107224.
[34] A. Xu, C. Dong, X. Wei, X. Li, D.D. Macdonald, The aggression behavior study of Cl− on the defect structure of passive films on copper, RSC Adv. 9 (2019) 15772–15779, https://doi.org/10.1039/C9RA03402A.
[35] D.M. Bastidas, B. Valdez, M. Schorr, J.M. Bastidas, Corrosion of copper intrauterine devices: review and recent developments, Corrosion Rev. 37 (2019) 307–320, https://doi.org/10.1515/corrrev-2019-0012.
[36] Y. Yang, K. Wang, X. Gu, K.W. Leong, Biophysical regulation of cell behavior—cross talk between substrate stiffness and nanotopography, Engineering 3 (2017) 36–54, https://doi.org/10.1016/J.ENG.2017.01.014.
[37] P. Yin Yee Chin, Q. Cheok, A. Glowacz, W. Caesarendra, A review of In-Vivo and In-Vitro real-time corrosion monitoring systems of biodegradable metal implants, Appl. Sci. 10 (2020) 3141, https://doi.org/10.3390/app10093141.
[38] M. Rahmati, M. Mozafari, A critical review on the cellular and molecular interactions at the interface of zirconia-based biomaterials, Ceram. Int. 44 (2018) 16137–16149, https://doi.org/10.1016/j.ceramint.2018.06.196.
[39] S. Long, J. Zhu, Y. Jing, S. He, L. Cheng, Z. Shi, A comprehensive review of surface modification techniques for enhancing the biocompatibility of 3D-Printed titanium implants, Coatings 13 (2023) 1917, https://doi.org/10.3390/coatings13111917.
[40] P. Jiang, Y. Zhang, R. Hu, B. Shi, L. Zhang, Q. Huang, Y. Yang, P. Tang, C. Lin, Advanced surface engineering of titanium materials for biomedical applications: from static modification to dynamic responsive regulation, Bioact. Mater. 27 (2023) 15–57, https://doi.org/10.1016/j.bioactmat.2023.03.006.
[41] C.R. Ferreira, W.A. Gahl, Disorders of metal metabolism, Transl. Sci. Rare Dis. 2 (2017) 101–139, https://doi.org/10.3233/TRD-170015.
[42] K. Jomova, S.Y. Alomar, E. Nepovimova, K. Kuca, M. Valko, Heavy metals: toxicity and human health effects, Arch. Toxicol. 99 (2025) 153–209, https://doi.org/10.1007/s00204-024-03903-2.
[43] P.D. Rakowska, M. Tiddia, N. Faruqui, C. Bankier, Y. Pei, A.J. Pollard, J. Zhang, I. S. Gilmore, Antiviral surfaces and coatings and their mechanisms of action, Commun. Mater. 2 (2021) 1–19, https://doi.org/10.1038/s43246-021-00153-y.
[44] Atomic weights of the elements 1993, Pure Appl. Chem. 66 (1994) 2423–2444, https://doi.org/10.1351/pac199466122423.
[45] T. Nagase, Y. Iijima, A. Matsugaki, K. Ameyama, T. Nakano, Design and fabrication of Ti–Zr-Hf-Cr-Mo and Ti–Zr-Hf-Co-Cr-Mo high-entropy alloys as metallic biomaterials, Mater. Sci. Eng. C 107 (2020) 110322, https://doi.org/10.1016/j.msec.2019.110322.
[46] O.N. Senkov, J.D. Miller, D.B. Miracle, C. Woodward, Accelerated exploration of multi-principal element alloys with solid solution phases, Nat. Commun. 6 (2015) 6529, https://doi.org/10.1038/ncomms7529.
[47] D.B. Miracle, O.N. Senkov, A critical review of high entropy alloys and related concepts, Acta Mater. 122 (2017) 448–511, https://doi.org/10.1016/j.actamat.2016.08.081.
[48] Y. Zhang, T.T. Zuo, Z. Tang, M.C. Gao, K.A. Dahmen, P.K. Liaw, Z.P. Lu, Microstructures and properties of high-entropy alloys, Prog. Mater. Sci. 61 (2014) 1–93, https://doi.org/10.1016/j.pmatsci.2013.10.001.
[49] A.K. Singh, N. Kumar, A. Dwivedi, A. Subramaniam, A geometrical parameter for the formation of disordered solid solutions in multi-component alloys, Intermetallics 53 (2014) 112–119, https://doi.org/10.1016/j.intermet.2014.04.019.
[50] Z. Wang, Y. Huang, Y. Yang, J. Wang, C.T. Liu, Atomic-size effect and solid solubility of multicomponent alloys, Scr. Mater. 94 (2015) 28–31, https://doi.org/10.1016/j.scriptamat.2014.09.010.
[51] S. Guo, Q. Hu, C. Ng, C.T. Liu, More than entropy in high-entropy alloys: forming solid solutions or amorphous phase, Intermetallics 41 (2013) 96–103, https://doi.org/10.1016/j.intermet.2013.05.002.
[52] X. Yang, Y. Zhang, Prediction of high-entropy stabilized solid-solution in multi-component alloys, Mater. Chem. Phys. 132 (2012) 233–238, https://doi.org/10.1016/j.matchemphys.2011.11.021.
[53] E.F. Daniel, C. Wang, C. Li, J. Dong, D. Zhang, W. Zhong, S. Zhong, I.I. Udoh, P. C. Okafor, Synergistic effect of crevice corrosion and galvanic coupling on 304SS fasteners degradation in chloride environments, npj Mater. Degrad. 7 (2023) 11, https://doi.org/10.1038/s41529-023-00327-8.
[54] F.A. Shah, P. Thomsen, A. Palmquist, Osseointegration and current interpretations of the bone-implant interface, Acta Biomater. 84 (2019) 1–15, https://doi.org/10.1016/j.actbio.2018.11.018.
[55] T. Ishimoto, Y. Kobayashi, M. Takahata, M. Ito, A. Matsugaki, H. Takahashi, R. Watanabe, T. Inoue, T. Matsuzaka, R. Ozasa, T. Hanawa, K. Yokota, Y. Nakashima, T. Nakano, Outstanding in vivo mechanical integrity of additively manufactured spinal cages with a novel “honeycomb tree structure” design via guiding bone matrix orientation, Spine J. 22 (2022) 1742–1757, https://doi.org/10.1016/j.spinee.2022.05.006.
[56] A. Matsugaki, M. Ito, Y. Kobayashi, T. Matsuzaka, R. Ozasa, T. Ishimoto, H. Takahashi, R. Watanabe, T. Inoue, K. Yokota, Y. Nakashima, T. Kaito, S. Okada, T. Hanawa, Y. Matsuyama, M. Matsumoto, H. Taneichi, T. Nakano, Innovative design of bone quality-targeted intervertebral spacer: accelerated functional fusion guiding oriented collagen and apatite microstructure without autologous bone graft, Spine J. 23 (2023) 609–620, https://doi.org/10.1016/j.spinee.2022.12.011.
[57] T. Matsuzaka, A. Matsugaki, K. Ishihara, T. Nakano, Osteogenic tailoring of oriented bone matrix organization using On/Off micropatterning for osteoblast adhesion on titanium surfaces, Acta Biomater. 192 (2025) 487–500, https://doi.org/10.1016/j.actbio.2024.12.017.